

# Intermediate Phase Modulation via Bifunctional Molecular Additive for High-Performance Quasi-2D Perovskite Photodetectors

Siliang Hu, Yi Shen, Haifan Li, Boxiang Gao, Xiaoguang Hu, Yuxuan Zhang, Weijun Wang, Mingqi Ding, Man Luo, Xiangpeng Kong, Chun-Yuen Wong, and Johnny C. Ho\*

Quasi-2D perovskite thin films hold great promise for creating highly efficient and stable optoelectronic devices. Regulating the intermediate phase during crystallization is crucial for determining film quality, directly impacting device performance. In this study, the bifunctional molecule L-carnitine is introduced into the quasi-2D precursor solution to modulate the intermediate phase during crystallization. The results demonstrate that the strong coordination between L-carnitine and  $\text{PbI}_2$  effectively impedes the combination of  $\text{PbI}_2$  and dimethyl sulfoxide (DMSO), preventing the formation of the  $\text{PbI}_2$ ·DMSO intermediate phase. This elimination of the intermediate phase mitigates the potential hazards associated with DMSO escape during subsequent annealing, significantly enhancing film quality. Furthermore, the bifunctional groups in L-carnitine interact with the perovskite, effectively passivating film defects and enhancing thermal and illumination stability. As a result, the L-carnitine-modified quasi-2D perovskite photodetector exhibits outstanding performance, with a responsivity of  $2724 \text{ mA W}^{-1}$  and a detectivity of  $9.10 \times 10^{10}$  Jones. This research proposes a novel strategy to regulate intermediate phases during crystallization and passivate defects synergistically, enabling the production of high-quality perovskite films and high-performance perovskite optoelectronic devices.

as a new generation of star semiconductor materials due to their exceptional properties, including high light absorption coefficients, long carrier lifetimes, and low preparation costs.<sup>[1–3]</sup> However, their commercialization is hindered by their susceptibility to decomposition under high humidity, temperature, and intense light, as they belong to a class of soft lattice materials.<sup>[4,5]</sup> To address this issue, converting 3D perovskites into quasi-2D structures by introducing organic cations with excellent hydrophobicity and thermal stability, such as diphenylpropylammonium (DPPA) and phenylethylammonium (PEA), can effectively enhance material stability.<sup>[6,7]</sup> Despite this improvement, the dielectric constant mismatch between organic and inorganic layers creates quantum wells, which impede charge carrier transport and subsequently affect device performance.<sup>[8]</sup> Polycyclic aromatic cations, like 1-naphthylmethylamine (NMA), often exhibit higher dielectric constants due to their greater polarity, effectively mitigating

## 1. Introduction

Metal halide perovskite materials ( $\text{ABX}_3$ , where A is a monovalent cation, B is a divalent cation, and X is a halogen) are regarded

the quantum confinement effect and enhancing the overall device efficiency.<sup>[9,10]</sup>

In addition to selecting the optimized organic cations, the final device performance is heavily influenced by the quality of

S. Hu, Y. Shen, B. Gao, Y. Zhang, W. Wang, M. Ding, M. Luo, J. C. Ho  
Department of Materials Science and Engineering  
City University of Hong Kong  
Kowloon, Hong Kong SAR 999077, China  
E-mail: johnnyho@cityu.edu.hk

H. Li, C.-Y. Wong  
Department of Chemistry  
City University of Hong Kong  
Kowloon, Hong Kong SAR 999077, China  
X. Hu  
School of Materials Science and Engineering  
Zhengzhou University  
Zhengzhou 450001, China

The ORCID identification number(s) for the author(s) of this article can be found under <https://doi.org/10.1002/adfm.202412965>

DOI: 10.1002/adfm.202412965

M. Luo  
School of Microelectronics and School of Integrated Circuits  
School of Information Science and Technology  
Nantong University  
Nantong 226019, China

X. Kong  
Shandong Institute for Product Quality Inspection  
Jinan 250100, China

J. C. Ho  
State Key Laboratory of Terahertz and Millimeter Waves  
City University of Hong Kong  
Kowloon, Hong Kong SAR 999077, China

J. C. Ho  
Institute for Materials Chemistry and Engineering  
Kyushu University  
Fukuoka 816–8580, Japan

the fabricated quasi-2D perovskite films, which are closely tied to the crystallization process.<sup>[11]</sup> During the solution preparation of perovskite films, the intermediate phase formed by the coordination between perovskite precursors and solvent molecules profoundly impacts the crystallization process, significantly affecting the film quality.<sup>[12,13]</sup> N,N-dimethylformamide (DMF), and dimethyl sulfoxide (DMSO) are the most commonly used solvents in this method.<sup>[14]</sup> However, the weak coupling between DMF and precursors leads to rapid evaporation during crystallization, accelerating the process and degrading film quality.<sup>[15,16]</sup> In contrast, DMSO has been shown to effectively retard the crystallization process due to its strong coupling effect, promoting the formation of high-quality films.<sup>[17,18]</sup> Unfortunately, this strong coupling also results in the formation of stable intermediate phases during crystallization.<sup>[19–21]</sup> Most oversaturation triggers, such as anti-solvents, fail to remove these residual highly coordinated intermediate phase compounds, preventing the formation of a pure perovskite phase after high-temperature annealing.<sup>[22]</sup> Moreover, the high-temperature annealing process causes the decomposition of intermediate phases and the escape of solvent molecules, leading to numerous defects in the film.<sup>[18]</sup> These defects not only reduce device performance but also serve as pathways for ion migration, accelerating device degradation.<sup>[18,23,24]</sup> Therefore, there is a critical need to develop a simple and controllable strategy to hinder intermediate phase formation and avoid adverse effects on film quality and device performance.

In this work, we introduce a simple and effective method to impede intermediate phase formation during crystallization, enabling the preparation of high-quality perovskite films. We incorporate the natural bifunctional molecule L-carnitine into the quasi-2D perovskite (NMA)<sub>2</sub>(MA)<sub>3</sub>Pb<sub>4</sub>I<sub>13</sub> precursor solution using DMSO as the solvent. During the crystallization process, the PbI<sub>2</sub>·DMSO intermediate phase is eliminated due to the stronger coordination ability between L-carnitine and PbI<sub>2</sub>, which prevents the binding between PbI<sub>2</sub> and DMSO. This approach also mitigates defect formation caused by DMSO escape during subsequent high-temperature annealing, thus remarkably enhancing the film quality. Moreover, L-carnitine's bifunctional groups interact simultaneously with the X-site of the perovskite, resulting in improved thermal and illumination stability of the modified films. As a result, the performance of the L-carnitine-modified photodetector is significantly enhanced, achieving responsivity and detectivity values of up to 2724 mA W<sup>-1</sup> and 9.10 × 10<sup>10</sup> Jones, respectively. Our work provides a novel strategy for modulating quasi-2D perovskite intermediate phases to achieve high-quality perovskite films, thereby enhancing the performance of perovskite photodetectors.

## 2. Results and Discussion

### 2.1. Characterization of L-Carnitine-Modified Perovskite Films

The schematic diagram for preparing quasi-2D perovskite films based on NMA spacer cation (*n* = 4) is illustrated in Figure 1a. All the films were prepared on glass substrates via a one-step spin-coating method (refer to the Supporting Information for detailed preparation procedures). L-carnitine was added to the precursor solution at concentrations of 0, 0.03, 0.05, 0.08, and

0.1 mol L<sup>-1</sup>, with the resulting films recorded as control, 0.03, 0.05, 0.08, and 0.1, respectively. Subject to solubility limitations, the solution became turbid at the L-carnitine concentration of 0.15 mol L<sup>-1</sup>, as depicted in Figure S1 (Supporting Information). To investigate compositional differences among the different films, X-ray diffraction (XRD) was conducted (Figure 1b). The results show that all the films exhibit diffraction peaks ≈15° and 29°, corresponding to the (111) and (202) crystal planes of the quasi-2D perovskite films, respectively.<sup>[25]</sup> However, the control sample displays more complex diffraction peaks, including a distinct peak ≈10.5°, indicative of the PbI<sub>2</sub>·DMSO intermediate phase.<sup>[26]</sup> As the concentration of L-carnitine increases, the intensity of this peak diminishes and ultimately disappears at an addition of 0.1 mol L<sup>-1</sup>. A comparable phenomenon was observed in the UV–vis absorption result. As shown in Figure 1c, all the films exhibit absorption peaks corresponding to *n* = 1, 2, 3, and 3D phases, designating the mixed-phase nature of the quasi-2D perovskite films. Notably, the control and 0.03 films (made with the L-carnitine concentration of 0.03 mol L<sup>-1</sup>) also exhibit new absorption peaks ≈380 nm, corresponding to the PbI<sub>2</sub>·DMSO intermediate phase.<sup>[27]</sup> Furthermore, the 0.05 sample displayed the identical absorption edge as the 0.03 and control samples (illustrated by the yellow dotted lines), thereby indicating the presence of the PbI<sub>2</sub>·DMSO intermediate phase in the 0.05 sample.<sup>[28]</sup> As the L-carnitine concentration increases, the peak mentioned above disappears. The XRD and UV–vis absorption results indicate that L-carnitine addition impedes the formation of the PbI<sub>2</sub>·DMSO intermediate phase, resulting in a purer film composition.

Functional groups such as amino, hydroxyl, and carboxyl groups in the additives have been widely demonstrated to facilitate defect passivation in perovskite films, enhancing film quality.<sup>[11,29]</sup> Given its bifunctional nature, L-carnitine has the potential to passivate film defects effectively. Consequently, we proceeded to undertake a series of tests, including steady-state photoluminescence (PL), time-resolved photoluminescence (TRPL), and space-charge-limited current (SCLC), on the prepared perovskite films to evaluate the impact of L-carnitine on defect passivation. Spontaneous radiative recombination of trap states usually leads to redshift emission due to its low energy.<sup>[30,31]</sup> Figure 1d illustrates the PL spectra of the perovskite films, where the emission peaks of the fluorescence spectra become continuously larger together with a blue shift with increasing L-carnitine content, indicating that non-radiative recombination is effectively suppressed. Also, the TRPL results (Figure 1e) reveal that the carrier lifetime of the perovskite film increases from 24.83 ns (control) to 64.82 ns (0.03), 67.94 ns (0.05), 107.25 ns (0.08), and 120.87 ns (0.1) (the fitting data are presented in Table S1, Supporting Information). The prolonged carrier lifetime suggests a lower defect state density in the films. Furthermore, the results of the SCLC measurements are illustrated in Figure 1f, which can clearly distinguish the trap-filling area. At the outset of the trap-filling region, the trap-filling limit voltage (*V*<sub>TFL</sub>) can be read, which is proportional to the defect state density of the film by  $N_t = \frac{2\epsilon_0\epsilon_r V_{TFL}}{eL^2}$ , where *N*<sub>t</sub> is the defect density,  $\epsilon_0$  is the vacuum permittivity,  $\epsilon_r$  is the relative dielectric constant, *e* is the electron charge, and *L* is the length of the channel.<sup>[13]</sup> The *V*<sub>TFL</sub> of the control sample is 5.36 V, while that of the other samples decreases to 3.23 V (0.03), 2.72 V (0.05), 0.67 V (0.08), and 0.46 V (0.1),

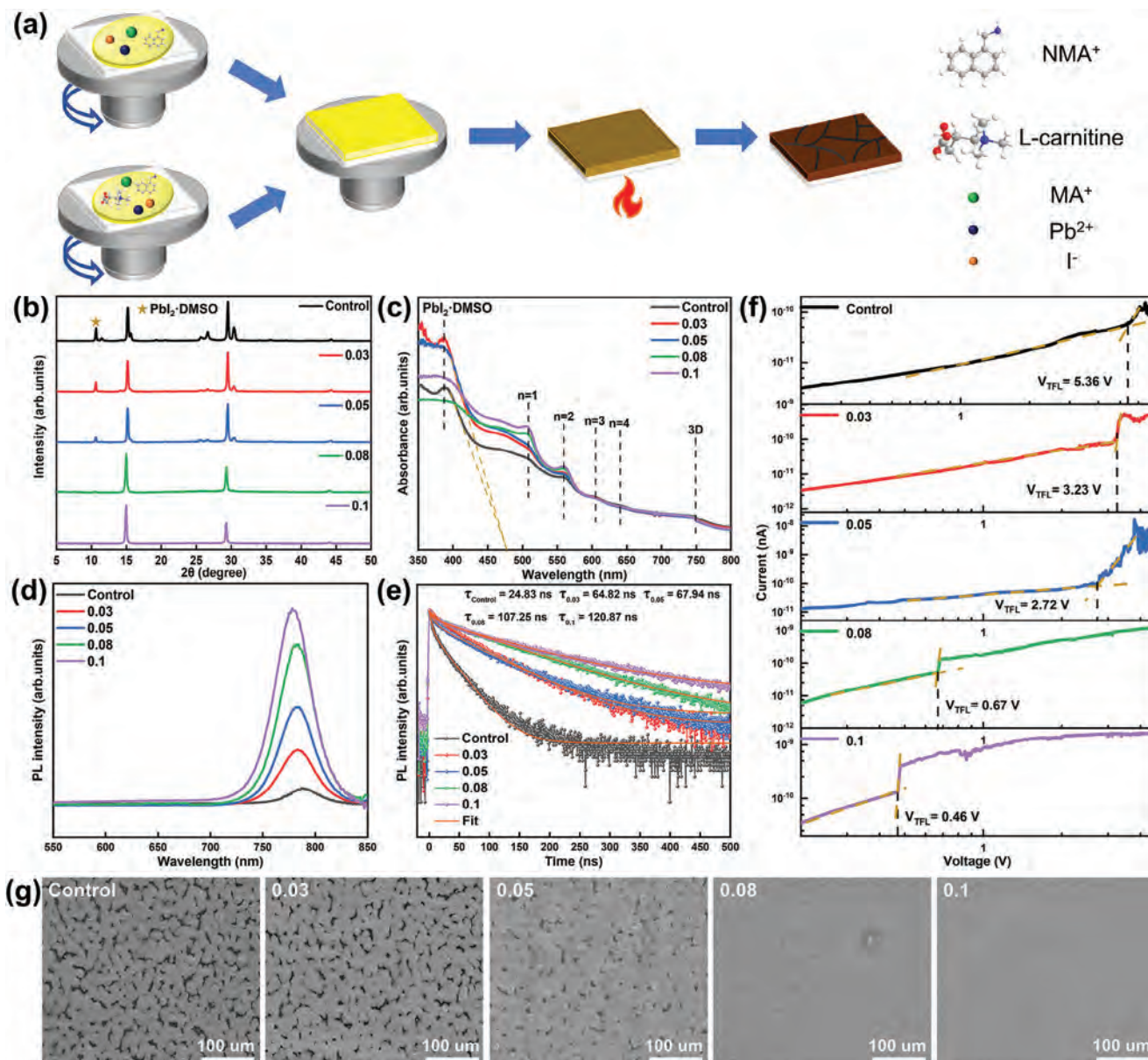


**Figure 1.** a) Schematic of the manufacturing process of the perovskite films. b) XRD patterns, c) absorption spectra, d) PL spectra, and e) TRPL spectra of the perovskite films made with different L-carnitine contents. f) I-V curves based on the SCLC test of the devices prepared from perovskite films with different L-carnitine contents. g) SEM images of the perovskite films with different L-carnitine contents.

respectively, inferring the reduced trap density in the perovskite films. These findings demonstrate that the L-carnitine molecule exerts an excellent passivation effect on the perovskite films, markedly enhancing their quality. To further investigate the changes in film quality, the micromorphology of the films was then characterized by scanning electron microscopy (SEM). As one can see in Figure 1g and Figure S2 (Supporting Information), the control film exhibits numerous conspicuous pinhole-like defects, accompanied by a notable deficiency in film coverage. Increasing the L-carnitine content decreases the number of defects gradually, and the film coverage improves. The defects nearly disappear after increasing the L-carnitine content above 0.08 mol L<sup>-1</sup>, resulting in dense and continuous films. These

observations are consistent with prior results, indicating that L-carnitine addition significantly enhances the perovskite film quality.

## 2.2. Mechanism for Enhancing the Quality of Perovskite Films

Previous studies have identified that the PbI<sub>2</sub>·DMSO intermediate phase decomposes into PbI<sub>2</sub> and releases DMSO when annealed at 80 °C.<sup>[26]</sup> Furthermore, the escape of DMSO from the films results in defect formation. Therefore, we hypothesize that the improvement in film quality also stems from the elimination of the PbI<sub>2</sub>·DMSO intermediate phase. To investigate the effect



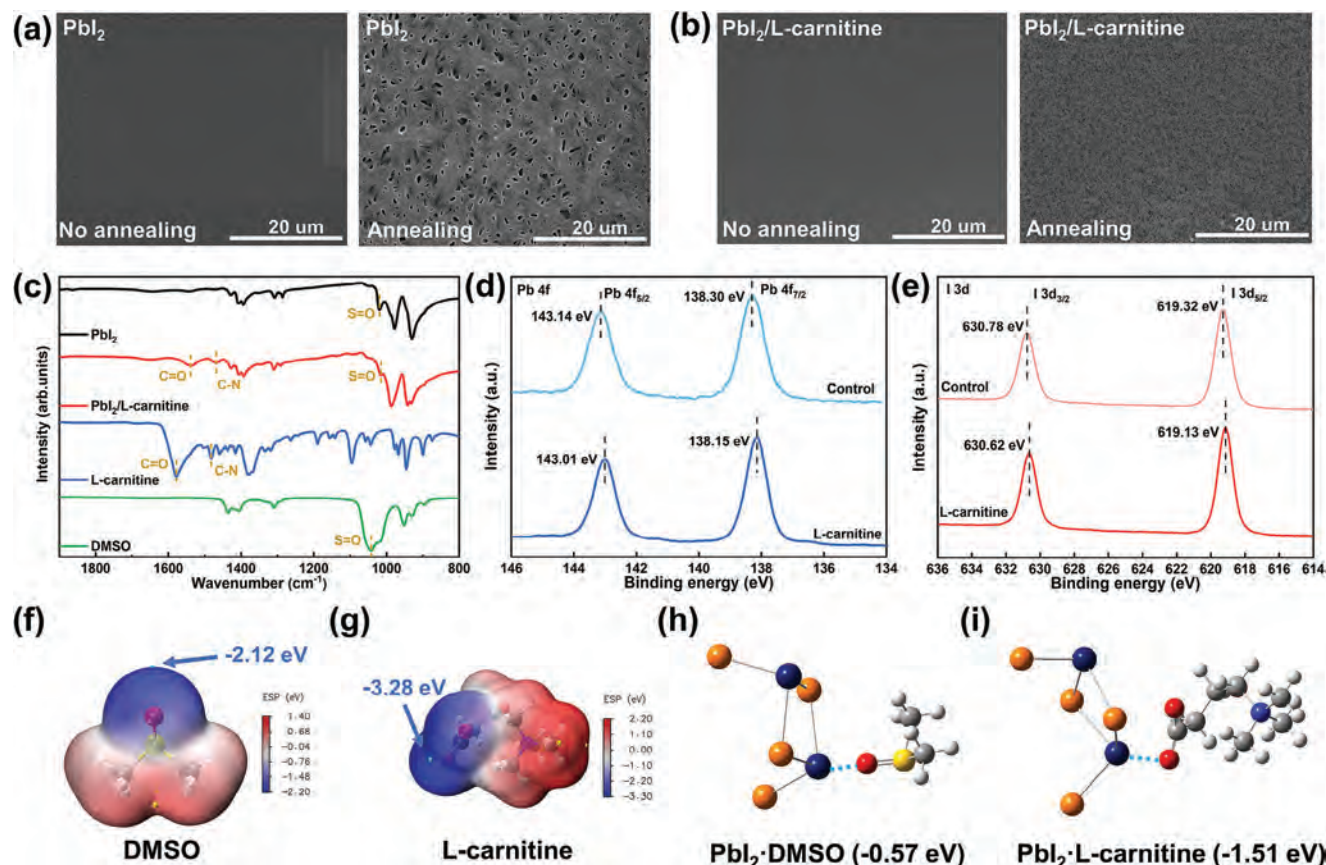


**Figure 2.** a) SEM images of the  $\text{PbI}_2$  precursor films before and after annealing. b) SEM images of the  $\text{PbI}_2/\text{L-carnitine}$  precursor films before and after annealing. c) FT-IR spectra of the  $\text{PbI}_2$ ,  $\text{PbI}_2/\text{L-carnitine}$ , and L-carnitine powder. XPS spectra of Pb 4f for control and L-carnitine-modified perovskite films d), I 3d for the control and L-carnitine-modified perovskite films e). Electrostatic potential surfaces for the DMSO molecule f) and L-carnitine molecule g). Schematic diagrams of the interactions of the  $\text{PbI}_2$  molecule with the DMSO molecule h) and the L-carnitine molecule i), respectively, and their corresponding binding energies.

of the  $\text{PbI}_2\cdot\text{DMSO}$  intermediate on the quality of the films, the micromorphology of pure  $\text{PbI}_2$  films and  $\text{PbI}_2/\text{L-carnitine}$  films was characterized before and after annealing, respectively. Before annealing, the pure  $\text{PbI}_2$  film exhibits a continuous morphology. However, numerous pinholes are observed in the film after annealing, as illustrated in **Figures 2a** and **S3** (Supporting Information). In contrast, the  $\text{PbI}_2/\text{L-carnitine}$  film maintains good coverage before and after annealing (Figure **2b**; Figure **S4**, Supporting Information). To investigate the reasons for the observed differences in film morphology, XRD and UV-vis absorption tests were employed to examine the compositional changes in pure  $\text{PbI}_2$  and  $\text{PbI}_2/\text{L-carnitine}$  films before and after annealing. The XRD results for pure  $\text{PbI}_2$  films are shown in Figure **S5** (Supporting Information), from which it can be seen that before annealing, the pure  $\text{PbI}_2$  film exhibits weak diffraction peaks for  $\text{PbI}_2$  and obvious diffraction peaks for the  $\text{PbI}_2\cdot\text{DMSO}$  intermediate phase. However, following annealing, the intensity of the  $\text{PbI}_2\cdot\text{DMSO}$  intermediate phase peaks significantly decreased, while the  $\text{PbI}_2$  peaks became more pronounced, indicating that a significant amount of DMSO escapes and converts the  $\text{PbI}_2\cdot\text{DMSO}$  intermediate phase to  $\text{PbI}_2$ . Conversely, the diffraction peaks of  $\text{PbI}_2$  are the only ones observed for the  $\text{PbI}_2/\text{L-carnitine}$  film both before and after annealing (Figure **S6**, Supporting Information). As

illustrated in Figure **S7** (Supporting Information), the UV-vis absorption test yielded comparable results. The pure  $\text{PbI}_2$  film still exhibits the absorption peak of the  $\text{PbI}_2\cdot\text{DMSO}$  intermediate phase, which is absent in the presence of L-carnitine. The SEM, XRD, and UV-vis characterization results prove that L-carnitine addition can enhance the quality of the perovskite films by impeding the formation of the  $\text{PbI}_2\cdot\text{DMSO}$  intermediate phase.

To shed light on the mechanism by which the  $\text{PbI}_2\cdot\text{DMSO}$  intermediate phase is eliminated under the assistance of L-carnitine, we conducted further investigation to ascertain the interaction among L-carnitine,  $\text{PbI}_2$ , and DMSO. The Fourier Transform Infrared (FT-IR) spectra of  $\text{PbI}_2$ ,  $\text{PbI}_2/\text{L-carnitine}$ , L-carnitine powder, and DMSO are presented in Figure **2c** and Figure **S8** (Supporting Information). A distinct feature of the stretching vibration peak at  $1042\text{ cm}^{-1}$  is observed for the DMSO sample, which correlates with the functional group of  $\text{S=O}$ , following the dissolution of  $\text{PbI}_2$  in DMSO and the preparation of the resulting powder, the characteristic  $\text{S=O}$  absorption peak exhibited a redshift to  $1019\text{ cm}^{-1}$ , indicating that DMSO coordinates with  $\text{PbI}_2$  and forms  $\text{PbI}_2\cdot\text{DMSO}$ ,<sup>[26]</sup> thus substantiating the existence of the  $\text{PbI}_2\cdot\text{DMSO}$  intermediate phase within the sample. When L-carnitine is added, the  $\text{S=O}$  bond stretching vibration peaks undergo a further redshift to  $1015\text{ cm}^{-1}$ ,

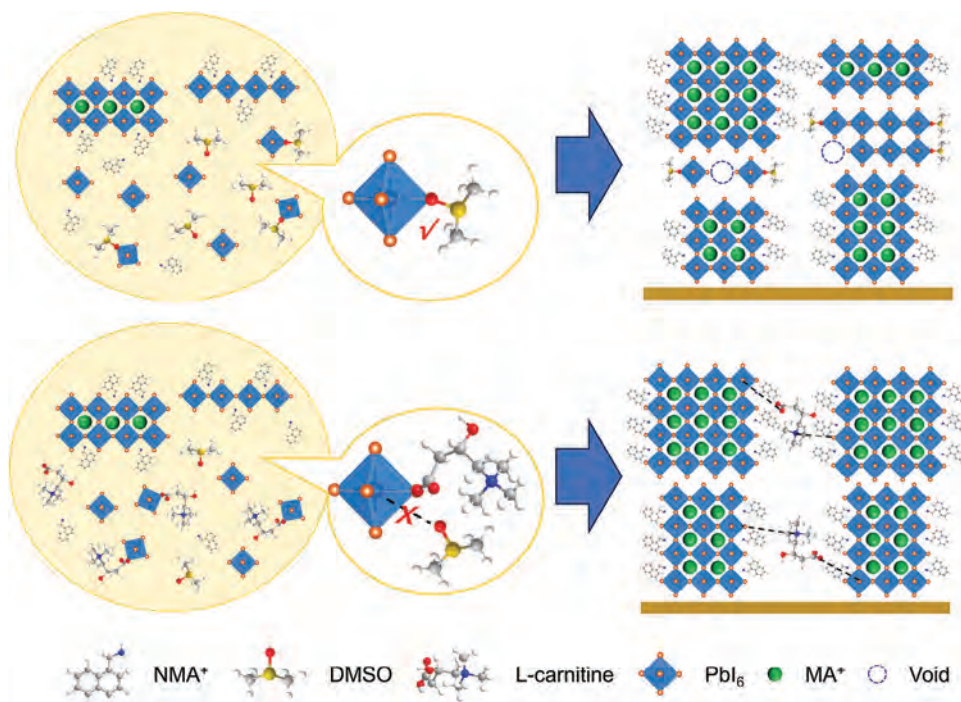


**Figure 3.** Schematic diagram of the effect of adding L-carnitine on the intermediate phase during perovskite crystallization and subsequent film growth.

accompanied by a notable reduction in the intensity of the vibration peaks. This suggests the existence of an interaction between L-carnitine and DMSO, which has resulted in the effective elimination of the  $\text{PbI}_2 \cdot \text{DMSO}$  intermediate phase. These findings are consistent with previous XRD and UV-vis absorption results. In addition, the feature of the stretching vibration peaks associated with the C–N and C=O is observed in both  $\text{PbI}_2/\text{L-carnitine}$  and L-carnitine samples. Following the addition of L-carnitine, the stretching vibration peaks of C–N and C=O exhibit a redshift from 1482 to 1469  $\text{cm}^{-1}$  and 1578 to 1540  $\text{cm}^{-1}$ , respectively. The apparent blueshift of these peaks can be attributed to the averaging of electron densities due to interactions between L-carnitine and  $\text{PbI}_2$ , in which C=O coordinates with  $\text{Pb}^{2+}$  and the quaternary ammonium group interacts with  $\text{I}^-$  through hydrogen bonding.<sup>[32,33]</sup> The X-ray Photoelectron Spectroscopy (XPS) experiments further confirmed the interactions between L-carnitine and  $\text{PbI}_2$ . The Pb 4f peaks for both control and L-carnitine-modified perovskite films are depicted in Figure 2d, where it can be observed that both films exhibit a doublet peak, which corresponds to  $\text{Pb}^{2+}$  4f<sub>5/2</sub> and 4f<sub>7/2</sub>, respectively. The peak signals for the control film are located at 138.30 and 143.14 eV, respectively. Upon the addition of L-carnitine, the peaks are all shifted to a lower binding energy, with peaks observed at 138.15 and 143.01 eV. A similar trend is observed in the shift of the I 3d signals (Figure 2e), where the peaks of the I<sup>−</sup> 3d<sub>3/2</sub> and 3d<sub>5/2</sub> signals move to 630.62 and 619.13 eV, respectively, from 630.78 and 619.32 eV, following the addition of L-carnitine. The above results suggest the chemical environment around the Pb and I atoms changed after L-carnitine addition, caused by the interaction among L-carnitine and the Pb, I atoms, which is consistent with the results of the FT-IR analysis. The FT-IR and XPS results showed that  $\text{PbI}_2$  preferentially

binds to L-carnitine, which in turn impedes the binding of  $\text{PbI}_2$  and DMSO.

More importantly, to further understand why L-carnitine binds more readily to  $\text{PbI}_2$ , we conducted theoretical calculations to corroborate the interaction among  $\text{PbI}_2$ , DMSO, and L-carnitine. First, the electrostatic potentials (ESP) of the DMSO and L-carnitine molecules were simulated to assess their ability to coordinate with  $\text{Pb}^{2+}$ . The ESP surfaces show the charge distributions of the two molecules in 3D (Figures 2f,g), thus enabling the visualization of the different charged regions. The blue coloration (negative potential) is observed when the atom is negatively charged near the outer edge. Previous studies have demonstrated that the region exhibiting a negative potential is optimal for coordination with positively charged  $\text{Pb}^{2+}$ . Moreover, the study has also shown that, in general, the lower the ESP in this region, the better the coordination capability.<sup>[34]</sup> The figure illustrates that both the S=O in the DMSO molecule and the C=O in the L-carnitine molecule exhibit significant negative potential regions. However, a comparison of the electrostatic potential around the C=O in the L-carnitine molecule (−3.28 eV) with that of the S=O in the DMSO molecule (−2.12 eV) reveals a smaller value for the former, indicating that the L-carnitine molecule exhibits much stronger coordination with  $\text{Pb}^{2+}$ . Then, we calculated the binding energies between  $\text{PbI}_2$  and DMSO, as well as  $\text{PbI}_2$  and L-carnitine, separately, as shown in Figures 2h,i. The binding energy of  $\text{PbI}_2 \cdot \text{L-carnitine}$  is −1.51 eV, which is significantly larger than that of  $\text{PbI}_2 \cdot \text{DMSO}$  (−0.57 eV), suggesting that the product formed by the combination of  $\text{PbI}_2$  and L-carnitine is more stable. This result again indicates the  $\text{PbI}_2$  molecules are more inclined to bind with L-carnitine than DMSO.

Based on the above analyses, a schematic diagram, illustrated in Figure 3, has been constructed to elucidate the



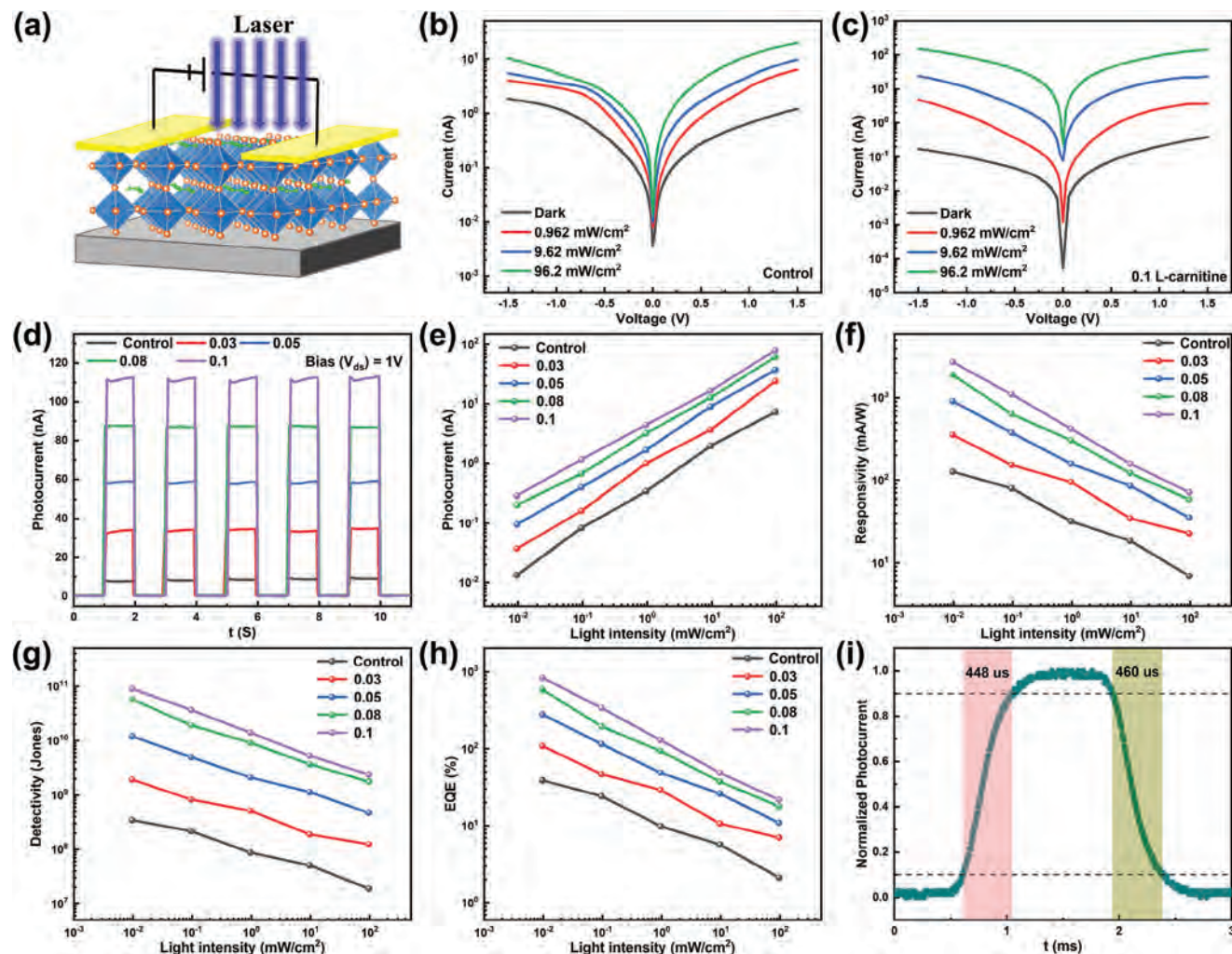


**Figure 4.** a) Schematic of the perovskite photodetector structure. I–V curves of the photodetector device without b) and with 0.1 mol L<sup>−1</sup> L-carnitine addition c). d) Time-dependent on-off switching characteristics of the perovskite devices prepared from perovskite films with different L-carnitine contents. Dependence of e) photocurrent, f) responsivity, g) detectivity, and h) EQE on the light intensity of the perovskite devices prepared from perovskite films with different L-carnitine contents. i) High-resolution current versus time curve for the L-carnitine-modified perovskite photodetector.

regulation mechanism of the intermediate phase by the L-carnitine molecule during the crystallization of perovskite films. Without L-carnitine molecules, the DMSO molecule coordinates with Pb<sup>2+</sup> through S=O—Pb bonding, forming the PbI<sub>2</sub>·DMSO intermediate phase, which is stable and challenging to remove during spin coating, resulting in its residual presence in the film. During the subsequent high-temperature annealing process, part of the DMSO molecule escapes, forming pinhole defects that damage the film quality. Following the addition of the L-carnitine molecule, the combination of the DMSO molecule and Pb<sup>2+</sup> is impeded due to the stronger coordination ability of the former with Pb<sup>2+</sup>. As a result, the DMSO molecule is effectively eliminated before annealing. Concurrently, the quaternary amine groups in the L-carnitine molecule interact with I<sup>−</sup>, thereby enhancing the structural stability of the perovskite. As a result, the L-carnitine's bifunctional groups interact with the perovskite, impeding the intermediate phase formation and passivating the defects, ultimately forming a high-quality perovskite film.

### 2.3. Performance and Stability of the Perovskite Photodetectors

To demonstrate the improvement in the photoelectric performance of L-carnitine-modified perovskite films, we fabricated the control, 0.03, 0.05, 0.08 and 0.1 film samples into photodetectors with the structure of glass/quasi-2D perovskite/Au (Figure 4a). Figure S9 (Supporting Information) illustrates the XRD patterns of the various films observed at angles below 10°. It is evident that all the films exhibit distinct diffraction peaks, which can be attributed to (0k0) diffraction peaks. This suggests that a proportion of the layered corner-sharing [PbI<sub>6</sub>]<sup>4−</sup> sheets exhibit growth parallel to the substrate.<sup>[35,36]</sup> This horizontal growth orientation facilitates charge transport in the horizontal devices that were prepared. The photoelectric properties of these devices were characterized using a 450 nm laser as the light source. Figures 4b,c and Figure S10 (Supporting Information) display the I–V characteristic curves under varying light intensities. The control sample only exhibits an on/off ratio of ≈10. This on/off ratio increased

**Table 1.** Summary of various figures of merits of 2D perovskite photodetectors.

Perovskites	Bias [V]	On/off ratio	R [mA W <sup>-1</sup> ]	D* [Jones]	Rise/decay time [ms]	Refs.
(iBA) <sub>2</sub> ((MA <sub>0.4</sub> FA <sub>0.6</sub> ) <sub>0.9</sub> CS <sub>0.1</sub> ) <sub>3</sub> Pb <sub>4</sub> I <sub>13</sub>	1.5	720	400	<sup>a)</sup> 1.68 × 10 <sup>12</sup>	43/22	[41]
(iBA) <sub>2</sub> (MA) <sub>n-1</sub> Pb <sub>n</sub> I <sub>3n+1</sub>	1.5	400	117	N/A	16/15	[42]
(C <sub>4</sub> H <sub>9</sub> NH <sub>3</sub> ) <sub>2</sub> (MA) <sub>2</sub> Pb <sub>3</sub> Br <sub>10</sub>	5	2.5 × 10 <sup>3</sup>	N/A	<sup>a)</sup> 3.6 × 10 <sup>10</sup>	0.15/0.57	[43]
(C <sub>5</sub> H <sub>11</sub> NH <sub>3</sub> ) <sub>2</sub> (MA) <sub>2</sub> Pb <sub>2</sub> I <sub>7</sub>	9.5	1 × 10 <sup>3</sup>	3.87	<sup>a)</sup> 2.92 × 10 <sup>10</sup>	0.0015/0.0017	[44]
(PEA) <sub>2</sub> PbI <sub>4</sub>	5	10.8	5.4	<sup>a)</sup> 1.07 × 10 <sup>13</sup>	N/A	[45]
(R)-α(PEA) <sub>2</sub> PbI <sub>4</sub>	3	124	600	<sup>b)</sup> 3.06 × 10 <sup>11</sup>	22/34	[46]
(C <sub>4</sub> H <sub>9</sub> NH <sub>3</sub> ) <sub>n</sub> (MA) <sub>n-1</sub> Pb <sub>n</sub> I <sub>3n+1</sub>	1	1 × 10 <sup>4</sup>	N/A	<sup>a)</sup> 10 <sup>11</sup> –10 <sup>12</sup>	0.002/0.004	[47]
(C <sub>6</sub> H <sub>5</sub> (CH <sub>2</sub> ) <sub>3</sub> NH <sub>3</sub> ) <sub>3</sub> Pb <sub>2</sub> I <sub>7</sub>	5	N/A	N/A	<sup>a)</sup> 1.2 × 10 <sup>10</sup>	0.85/0.78	[48]
[(R)-βMPA] <sub>2</sub> MAPb <sub>2</sub> I <sub>7</sub>	10	N/A	1100	<sup>b)</sup> 2.3 × 10 <sup>11</sup>	3.5/4.9	[49]
DMPDAPbI <sub>4</sub>	1.5	3.3 × 10 <sup>4</sup>	893	<sup>a)</sup> 2.4 × 10 <sup>12</sup>	0.446/0.420	[50]
(BA) <sub>2</sub> (MA) <sub>n-1</sub> Pb <sub>n</sub> I <sub>3n+1</sub>	2	N/A	<30	<sup>a)</sup> 5 × 10 <sup>8</sup>	10/10	[51]
(NMA) <sub>2</sub> (MA) <sub>3</sub> Pb <sub>4</sub> I <sub>13</sub>	1	1 × 10 <sup>3</sup>	2724	<sup>b)</sup> 9.10 × 10 <sup>10</sup>	0.448/0.460	This work

Note: Different formula for calculating detectivity ( $D^*$ ): <sup>a)</sup>  $D^* = RS^{1/2}/(2eI_{\text{dark}})^{1/2}$ , where  $e$  is the electronic charge,  $S$  is the effective area of the photodetector,  $R$  is the responsivity and  $I_{\text{dark}}$  is the dark current; <sup>b)</sup>  $D^* = D^* = S^{1/2}/NEP$ , where  $S$  is the effective area of the photodetector,  $NEP$  is the noise equivalent power which can be calculated by the formula of  $NEP = I_n/R$  ( $I_n$  is the current noise spectral density).

steadily with the addition of L-carnitine, reaching  $\approx 10^3$  when 0.1 mol L<sup>-1</sup> of L-carnitine was supplied. The observed increase in the on/off ratio is attributed to enhanced film quality, which, on the one hand, raises photocurrent under light source excitation. On the other hand, the removal of pinhole-like defects effectively lowers the dark current.<sup>[37]</sup> Figure 4d presents the dynamic photoresponse measured at a light intensity of 130 mW cm<sup>-2</sup> and a bias voltage of 1 V. The current–time (I–t) results demon-

strate that the photoswitching characteristics of all the perovskite photodetectors are stable and reversible. Besides, the photocurrent of the 0.1 sample is 16 times higher than that of the control sample, which can be attributed to the film's purer phase composition and fewer defects. Figure 4e shows the photocurrent at different light intensities, revealing a linear increase with rising light intensity. Additionally, responsivity ( $R$ ), detectivity ( $D^*$ ), and external quantum efficiency (EQE) are also crucial parameters

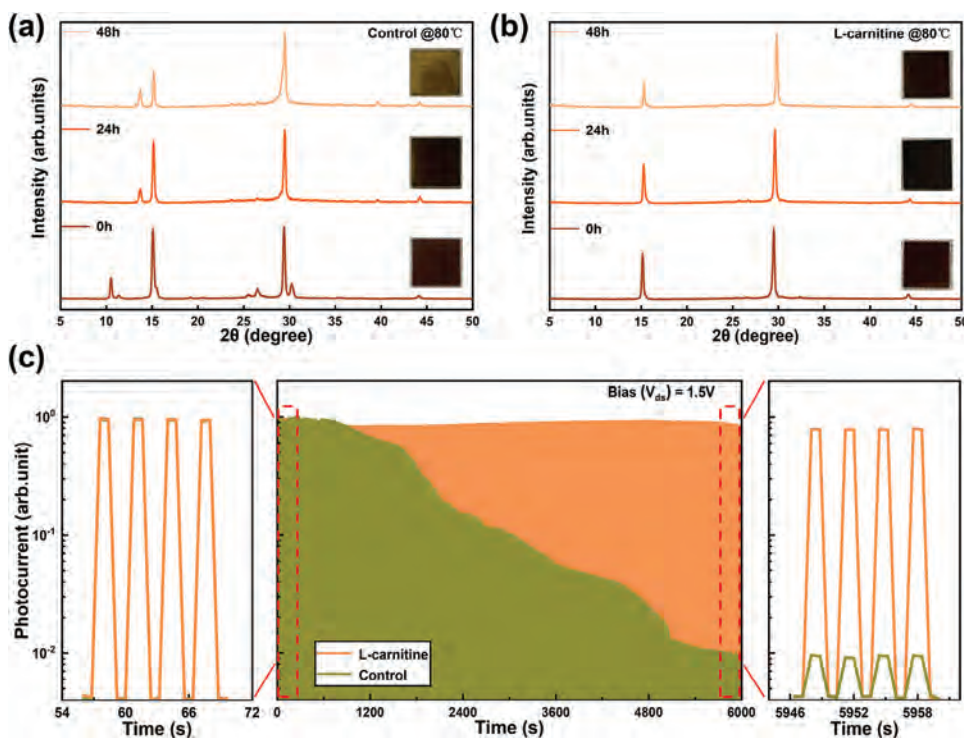


**Figure 5.** XRD patterns of the perovskite films without a) and with L-carnitine addition b) under 80 °C heating. Inset is the optical image of the films. c) Dependence of the photocurrent on the operation time of the photodetector device without and with L-carnitine addition.

for evaluating the photodetector's light detection capability. These parameters are calculated using the following equations:  $R = I_p / \Phi S$ ,  $D^* = S^{1/2} / NEP$ ,  $EQE = hcR / e\lambda$ , where  $I_p$  is the photocurrent ( $I_p = I_{\text{light}} - I_{\text{dark}}$ ),  $\Phi$  is the light intensity,  $S$  is the photodetector's active area,  $e$  is the electronic charge,  $I_{\text{dark}}$  is the dark current of the photodetector,  $NEP$  is the noise equivalent power which can be calculated by the formula of  $NEP = I_n / R$  ( $I_n$  is the current noise spectral density shown in Figure S11, Supporting Information),  $h$  is Planck's constant,  $c$  is the velocity of light, and  $\lambda$  is the wavelength of the laser. Figure 4f illustrates the device responsivity as a function of the irradiating light intensity. The modified devices exhibit higher responsivity at all light intensities, with the device of the 0.1 sample exhibiting an R-value of  $2724 \text{ mA W}^{-1}$  at a light intensity of  $0.00962 \text{ mW cm}^{-2}$ , which is much larger than that of the control sample device ( $126 \text{ mA W}^{-1}$ ). Similarly, the modified sample devices demonstrate superior  $D^*$  and EQE performance. As shown in Figures 4g,h, at a light intensity of  $0.00962 \text{ mW cm}^{-2}$ , the  $D^*$  and EQE for the 0.1 sample device are  $9.10 \times 10^{10}$  Jones and 835%, respectively, while the control sample device's  $D^*$  and EQE are only  $3.45 \times 10^8$  Jones and 39%, respectively. The enhanced device performance of the modified samples is due to the improved quality and purer phase composition of the perovskite film, which facilitates the generation and transport of photogenerated carriers. As evidenced by the changes in carrier mobility, by fitting the third segment (Child' region) of the SCLC curve (Figure S12, Supporting Information) with the formula of  $J = 9\epsilon\epsilon_0\mu V^2 / 8L^3$  where  $J$  is the current density,  $\epsilon$  is the relative dielectric constant ( $\epsilon = 25$ ),<sup>[38]</sup>  $\epsilon_0$  is the vacuum permittivity, and  $L$  is the length between two electrodes. The carrier mobility ( $\mu$ ) of the control and L-carnitine-modified films was found to be  $\approx 1.92 \times 10^{-2}$  and  $\approx 1.23 \times 10^{-1} \text{ cm}^2 \text{ V}^{-1} \text{ s}^{-1}$ , respectively. Moreover, the response time of the optimal device was characterized, as shown in Figure 4i, with rise and decay times (defined as current rising from 10 to 90% and falling from 90 to 10% of peak value) of 448 and 460  $\mu\text{s}$ , respectively. These results demonstrate that the performance of photodetector devices prepared with L-carnitine is significantly enhanced compared to those without it. Table 1 summarizes the performance of 2D perovskite photodetector devices comprising various components, which reveals that our devices prepared in this study exhibit excellent performance compared to other devices.

Furthermore, the poor stability of perovskite films is also a major obstacle limiting their further commercialization. Therefore, we evaluated the thermal and illumination stability of the control and the L-carnitine-modified samples. As shown in Figures 5a,b, which depict the XRD patterns of the two samples after continuous heating at  $80^\circ\text{C}$ . Figure 5a shows that after 24 h of continuous heating, the diffraction peaks of the  $\text{PbI}_2 \cdot \text{DMSO}$  intermediate phase disappear from the control samples' XRD patterns. Instead, the diffraction peaks of  $\text{PbI}_2$  reemerge, and its intensity increases as the heating time is extended. This result is consistent with the previous discussion of the decomposition of the  $\text{PbI}_2 \cdot \text{DMSO}$  intermediate phase into  $\text{PbI}_2$  at high temperatures. Conversely, following 48 h of continuous heating, the L-carnitine-modified perovskite film shows outstanding thermal stability, with no  $\text{PbI}_2$  peaks observed (Figure 5b). Afterward, the  $I$ - $t$  curves of the two devices were observed in an air environment for 6000 s, as indicated by Figure 5c, with a light intensity of  $130 \text{ mW cm}^{-2}$  and a bias voltage of 1.5 V. The photocur-

rent of the control sample device drops rapidly as the illumination time is extended. After 6000 s of illumination, the photocurrent is only  $\approx 10\%$  of its initial value. In contrast, the L-carnitine-modified device retains  $\approx 80\%$  of its initial photocurrent, indicating exceptional illumination stability. Also, an increase in performance has been observed with the passage of time during the test phase, which can be due to concomitant effects such as light or field-induced ion movement with the associated structural rearrangement, light-induced trap formation, or interfacial charge accumulation.<sup>[39,40]</sup> This evidence suggests that the L-carnitine-modified device has superior thermal and illumination stability compared to the control device due to tighter structural bonding facilitated by the interaction of the bifunctional groups of L-carnitine. Overall, the purer composition, lower defect density, and tighter structural bonding all contribute to improved device performance and stability.

### 3. Conclusion

In summary, we have introduced a novel additive molecule, L-carnitine, to modulate the intermediate phase during the crystallization of perovskite films, resulting in the fabrication of high-quality perovskite films and high-performance perovskite photodetector devices. The strong coordination between the  $\text{C}=\text{O}$  bond in L-carnitine and  $\text{Pb}^{2+}$  effectively impedes the coordination of DMSO with  $\text{Pb}^{2+}$ , thereby eliminating the residual  $\text{PbI}_2 \cdot \text{DMSO}$  intermediate phase in the film. Moreover, the bifunctional groups in L-carnitine effectively passivate defects, leading to films with low defect state density, pure phase composition, dense morphology, and excellent thermal and illumination stability. When configured into photodetectors, these L-carnitine-modified films exhibit impressive performance, with a high responsivity of  $2724 \text{ mA W}^{-1}$  and a detectivity of  $9.10 \times 10^{10}$  Jones. This work provides an effective strategy for modulating intermediate phases during perovskite crystallization, offering a novel approach to preparing high-quality perovskite films and enhancing the performance of perovskite optoelectronic devices.

### Supporting Information

Supporting Information is available from the Wiley Online Library or from the author.

### Acknowledgements

S.H. and Y.S. contributed equally to the work. This work was financially supported by the City University of Hong Kong (Project no. 7020088 and 7005944).

### Conflict of Interest

The authors declare no conflict of interest.

### Data Availability Statement

The data that support the findings of this study are available from the corresponding author upon reasonable request.



## Keywords

bifunctional molecular additive, intermediate phase modulation, photodetector, quasi-2D perovskite

Received: July 20, 2024

Revised: September 8, 2024

Published online: October 2, 2024

- [1] X. K. Liu, W. Xu, S. Bai, Y. Jin, J. Wang, R. H. Friend, F. Gao, *Nat. Mater.* **2021**, 20, 10.
- [2] A. Jana, S. Cho, S. A. Patil, A. Meena, Y. Jo, V. G. Sree, Y. Park, H. Kim, H. Im, R. A. Taylor, *Mater. Today* **2022**, 55, 110.
- [3] Y. Jiang, X. Wang, A. Pan, *Adv. Mater.* **2019**, 31, 1806671.
- [4] J. Zhang, X. Song, L. Wang, W. Huang, *Natl. Sci. Rev.* **2022**, 9, 129.
- [5] H. P. Wang, S. Li, X. Liu, Z. Shi, X. Fang, J. H. He, *Adv. Mater.* **2021**, 33, 2003309.
- [6] Y. C. Kim, H. J. An, D. H. Kim, J. M. Myoung, Y. J. Heo, J. H. Cho, *Adv. Funct. Mater.* **2020**, 31, 2005553.
- [7] Z. Li, Z. Chen, Y. Yang, Q. Xue, H. L. Yip, Y. Cao, *Nat. Commun.* **2019**, 10, 1027.
- [8] Q. Cao, P. Li, W. Chen, S. Zang, L. Han, Y. Zhang, Y. Song, *Nano Today* **2022**, 43, 101394.
- [9] Y. Liu, J. Guo, H. Zhou, C. Li, X. Guo, *J. Am. Chem. Soc.* **2024**, 146, 8198.
- [10] L. Zheng, L. Shen, Z. Fang, P. Song, W. Tian, J. Chen, K. Liu, Y. Luo, P. Xu, J. Yang, C. Tian, L. Xie, Z. Wei, *Adv. Energy Mater.* **2023**, 13, 2301066.
- [11] T. H. Han, S. Tan, J. Xue, L. Meng, J. W. Lee, Y. Yang, *Adv. Mater.* **2019**, 31, 1803515.
- [12] J. Cao, X. Jing, J. Yan, C. Hu, R. Chen, J. Yin, J. Li, N. Zheng, *J. Am. Chem. Soc.* **2016**, 138, 9919.
- [13] Y. Li, X. Guan, Y. Meng, J. Chen, J. Lin, X. Chen, C.-Y. Liu, Y. Zhao, Q. Zhang, C. Tian, J. Lu, Z. Wei, *InfoMat* **2024**, 6, 12537.
- [14] L. Chao, T. Niu, W. Gao, C. Ran, L. Song, Y. Chen, W. Huang, *Adv. Mater.* **2021**, 33, 2005410.
- [15] H. Chen, Q. Guan, H. Yan, X. Cui, Z. Shu, Y. Cai, *ACS Appl. Mater. Interfaces* **2023**, 15, 32475.
- [16] S. N. Manjunatha, Y.-X. Chu, M.-J. Jeng, L.-B. Chang, *J. Electron. Mater.* **2020**, 49, 6823.
- [17] N. J. Jeon, J. H. Noh, Y. C. Kim, W. S. Yang, S. Ryu, S. I. Seok, *Nat. Mater.* **2014**, 13, 897.
- [18] S. Chen, X. Dai, S. Xu, H. Jiao, L. Zhao, J. Huang, *Science* **2021**, 373, 902.
- [19] X. Du, J. Zhang, H. Su, X. Guo, Y. Hu, D. Liu, N. Yuan, J. Ding, L. Gao, S. F. Liu, *Adv. Mater.* **2022**, 34, 2204098.
- [20] P. Jia, G. Chen, G. Li, J. Liang, H. Guan, C. Wang, D. Pu, Y. Ge, X. Hu, H. Cui, S. Du, C. Liang, J. Liao, G. Xing, W. Ke, G. Fang, *Adv. Mater.* **2024**, 36, 2400105.
- [21] X. Zhao, Y. Qiu, M. Wang, D. Wu, X. Yue, H. Yan, B. Fan, S. Du, Y. Yang, Y. Yang, D. Li, P. Cui, H. Huang, Y. Li, N.-G. Park, M. Li, *ACS Energy Lett.* **2024**, 9, 2659.
- [22] W. Zuo, M. M. Byrannvand, T. Kodalle, M. Zohdi, J. Lim, B. Carlsen, T. Magorian Friedlmeier, M. Kot, C. Das, J. I. Flege, W. Zong, A. Abate, C. M. Sutter-Fella, M. Li, M. Saliba, *Adv. Mater.* **2023**, 35, 2302889.
- [23] A. Mei, Y. Sheng, Y. Ming, Y. Hu, Y. Rong, W. Zhang, S. Luo, G. Na, C. Tian, X. Hou, Y. Xiong, Z. Zhang, S. Liu, S. Uchida, T.-W. Kim, Y. Yuan, L. Zhang, Y. Zhou, H. Han, *Joule* **2020**, 4, 2646.
- [24] D. P. McMeekin, P. Holzhey, S. O. Furer, S. P. Harvey, L. T. Schelhas, J. M. Ball, S. Mahesh, S. Seo, N. Hawkins, J. Lu, M. B. Johnston, J. J. Berry, U. Bach, H. J. Snaith, *Nat. Mater.* **2023**, 22, 73.
- [25] Q. Fu, M. Chen, Q. Li, H. Liu, R. Wang, Y. Liu, *J. Am. Chem. Soc.* **2023**, 145, 21687.
- [26] W. Liu, T. Shi, J. Zhu, Z. Zhang, D. Li, X. He, X. Fan, L. Meng, J. Wang, R. He, Y. Ge, Y. Liu, P. K. Chu, X. F. Yu, *Adv. Sci.* **2022**, 10, 2204512.
- [27] W. Zha, L. Zhang, L. Wen, J. Kang, Q. Luo, Q. Chen, S. Yang, C.-Q. Ma, *Acta Phys.-Chim. Sin.* **2020**, 38, 2003022.
- [28] N. K. Kumawat, A. Dey, A. Kumar, S. P. Gopinathan, K. L. Narasimhan, D. Kabra, *ACS Appl. Mater. Interfaces* **2015**, 7, 13119.
- [29] M.-H. Park, J. S. Kim, J.-M. Heo, S. Ahn, S.-H. Jeong, T.-W. Lee, *ACS Energy Lett.* **2019**, 4, 1134.
- [30] S. Yang, J. Dai, Z. Yu, Y. Shao, Y. Zhou, X. Xiao, X. C. Zeng, J. Huang, *J. Am. Chem. Soc.* **2019**, 141, 5781.
- [31] S. Vidal, M. Izquierdo, S. Filippone, I. Fernandez, S. Akin, J. Y. Seo, S. M. Zakeeruddin, M. Gratzel, N. Martin, *Chem. Eur. J.* **2019**, 25, 3224.
- [32] L. Yang, H. Zhou, Y. Duan, M. Wu, K. He, Y. Li, D. Xu, H. Zou, S. Yang, Z. Fang, S. Liu, Z. Liu, *Adv. Mater.* **2023**, 35, 2211545.
- [33] H. C. Chen, C. M. Hung, C. H. Kuo, *ACS Appl. Mater. Interfaces* **2021**, 13, 8595.
- [34] L. Cai, F. Yang, Y. Xu, J. Fan, Y. Li, Y. Zhao, D. Liang, Y. Zou, P. Li, L. Wang, C. Wang, Y. Li, J. Fan, B. Sun, *ACS Appl. Mater. Interfaces* **2020**, 12, 37346.
- [35] H. Yao, Z. Li, C. Shi, Y. Xu, Q. Wang, Z. Li, G. Peng, Y. Lei, H. Wang, Z. Ci, Z. Jin, *Adv. Funct. Mater.* **2022**, 32, 2205029.
- [36] Z. Xu, D. Lu, X. Dong, M. Chen, Q. Fu, Y. Liu, *Adv. Mater.* **2021**, 33, 2105083.
- [37] H. Wang, S. Hu, H. Li, Y. Guo, G. Zhao, P. Liu, J. Gao, Z. Cheng, Y. Tong, H. Qi, Y. Zhang, H. Wang, *Org. Electron.* **2023**, 114, 106746.
- [38] Z. Xu, D. Lu, F. Liu, H. Lai, X. Wan, X. Zhang, Y. Liu, Y. Chen, *ACS Nano* **2020**, 14, 4871.
- [39] P. Gratia, G. Grancini, J. N. Audinot, X. Jeanbourquin, E. Mosconi, I. Zimmermann, D. Dowsett, Y. Lee, M. Gratzel, F. De Angelis, K. Sivula, T. Wirtz, M. K. Nazeeruddin, *J. Am. Chem. Soc.* **2016**, 138, 15821.
- [40] B. Saparov, D. B. Mitzi, *Chem. Rev.* **2016**, 116, 4558.
- [41] R. Dong, C. Lan, F. Li, S. Yip, J. C. Ho, *Nanoscale Horiz.* **2019**, 4, 1342.
- [42] R. Dong, C. Lan, X. Xu, X. Liang, X. Hu, D. Li, Z. Zhou, L. Shu, S. Yip, C. Li, S.-W. Tsang, J. C. Ho, *ACS Appl. Mater. Interfaces* **2018**, 10, 19019.
- [43] L. Li, Z. Sun, P. Wang, W. Hu, S. Wang, C. Ji, M. Hong, J. Luo, *Angew. Chem., Int. Ed.* **2017**, 56, 12150.
- [44] S. Han, P. Wang, J. Zhang, X. Liu, Z. Sun, X. Huang, L. Li, C. Ji, W. Zhang, B. Teng, W. Hu, M. Hong, J. Luo, *Laser Photonics Rev.* **2018**, 12, 1800060.
- [45] C.-H. Lin, B. Cheng, T.-Y. Li, J. R. D. Retamal, T.-C. Wei, H.-C. Fu, X. Fang, J.-H. He, *ACS Nano* **2019**, 13, 1168.
- [46] J. Wang, C. Fang, J. Ma, S. Wang, L. Jin, W. Li, D. Li, *ACS Nano* **2019**, 13, 9473.
- [47] K. Wang, C. Wu, D. Yang, Y. Jiang, S. Priya, *ACS Nano* **2018**, 12, 4919.
- [48] X. Fu, S. Jiao, Y. Jiang, L. Li, X. Wang, C. Zhu, C. Ma, H. Zhao, Z. Xu, Y. Liu, W. Huang, W. Zheng, P. Fan, F. Jiang, D. Zhang, X. Zhu, X. Wang, A. Pan, *ACS Appl. Mater. Interfaces* **2020**, 12, 2884.
- [49] L. Wang, Y. Xue, M. Cui, Y. Huang, H. Xu, C. Qin, J. Yang, H. Dai, M. Yuan, *Angew. Chem., Int. Ed.* **2020**, 59, 6504.
- [50] Z. Lai, Z. Zeng, Y. Meng, Y. Zhang, Y. Shen, W. Wang, D. Li, D. Chen, D. Yin, S.-W. Tsang, S. Yip, J. C. Ho, *Adv. Funct. Mater.* **2023**, 33, 2305539.
- [51] Q. Fu, X. Wang, F. Liu, Y. Dong, Z. Liu, S. Zheng, A. Chaturvedi, J. Zhou, P. Hu, Z. Zhu, F. Bo, Y. Long, Z. Liu, *Small* **2019**, 15, 1902890.